Volume 7 | Number 9 | 7 May 2023

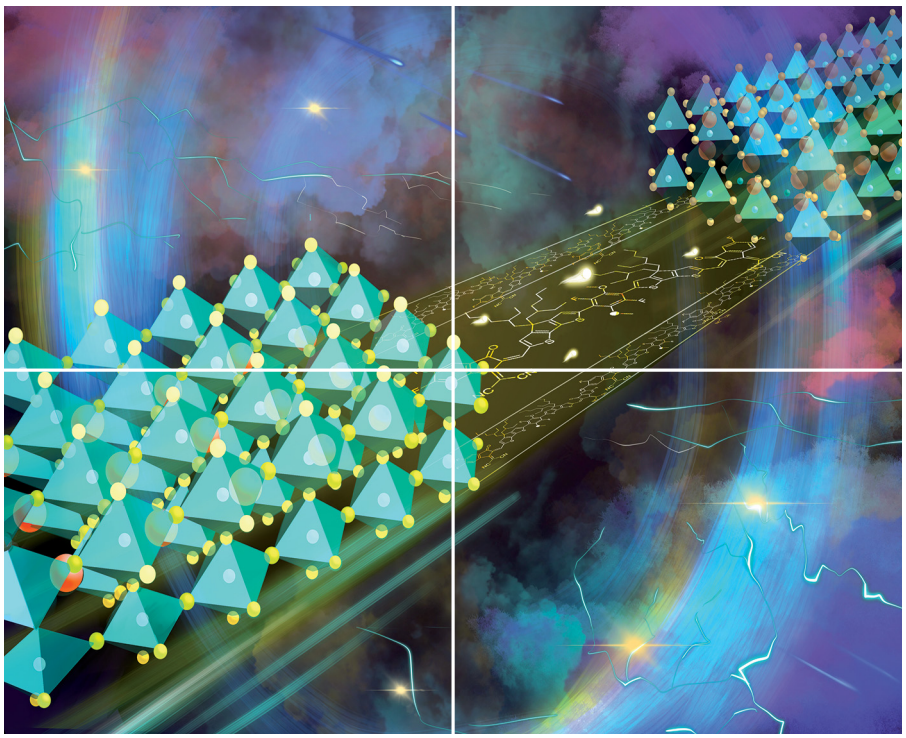

MATERIALS CHEMISTRY

FRONTIERS

CCS 中国化学会 CHINESE CHEMICAL SOCIETY

ICCAS 1956

ROYAL SOCIETY OF CHEMISTRY

rsc.li/frontiers-materials

MATERIALS CHEMISTRY FRONTIERS

RESEARCH ARTICLE

View Article Online
View Journal | View Issue

Cite this: *Mater. Chem. Front.*, 2023, 7, 1803

Bridging the inter-grain charge transport *via* organic semiconductors for high-performance thickness-insensitive perovskite solar cells†

Yuying Cao, [ab] Fei Wu,[a] Chang Xu,[a] Haotian Wu,[a] Shuixing Li,[a] Xinru Wang,[a] Tianyi Chen,[a] Boyu Peng, [a] Hanying Li, [a] Hongzheng Chen *[a] and Lijian Zuo *[ab]

The solution-processability of perovskite solar cells (PVSCs) reduces the production cost, but renders a multi-crystalline film with a large number of grain boundaries, which hinders the charge transport and induces defects. In this work, we have studied the potential of organic semiconductors for remedying the grain boundaries of perovskite films. Non-fullerene acceptors (NFAs) of different energy levels have been filled into the grain boundaries of perovskite films to form different energetic structures. It is unveiled that constructing a "flat-band" quantum well structure (FBQW, where the highest occupied molecular orbital and lowest unoccupied molecular orbital align with the valence band and conductance band, respectively), can effectively bridge the charge transport at the grain boundaries. As a result, the NFA, *i.e.*, HFO-PCIC can obviously reduce the series resistance and enable the best device performance of over 21% based on $MAPbI_3$ solar cells. Moreover, constructing a FBQW at the grain boundary almost fully retains the device efficiency (20.7% for the best) with a perovskite thickness over 1500 nm, which is the best result among thick PVSCs. With the thickness-insensitive merit, the fabrication of perovskites will be more tolerant to the processing conditions toward practical application. Therefore, the FBQW proposed in this work can effectively remedy inter-grain charge transport for high device performance and should pave the way for thickness-insensitive perovskite solar cells for future commercialization of PVSCs.

Received 31st December 2022,
Accepted 8th March 2023

DOI: 10.1039/d2qm01376b

rsc.li/frontiers-materials

Introduction

Hybrid organic–inorganic metal halide perovskites solar cells (PVSCs) possess exceptional optoelectronic properties, high absorption coefficients, long carrier diffusion lengths, superb charge carrier mobilities, and tunable bandgaps that make them attract paramount interest from the research community.[1–10] Up to now, the power conversion efficiency (PCE) of PVSCs with single-junction 3D cells has been dramatically enhanced from 3.8% in 2009 to over 25%, which qualifies it to compete with silicon solar cells in the future PV market.[11–16] At the same time, the solution processing of PVSCs offers an additional advantage for fabricating high-efficiency PVSC devices at a low cost. These achievements accelerate the pace of commercialization. However, the solution processing of perovskite film induces a multi-crystalline film, which will produce a large number of grain boundaries in the active layer and unpredictable surface morphology.[17,18] Obviously, preparing a perovskite film with good uniformity, pinhole-free texture, and high crystallinity is vital to achieve high performance for PVSCs, because the rough surface and pin-holes of the perovskite active layer will cause a severe leakage current, and the low crystallinity will cause high resistance and low charge collection efficiency.[19] Various modification strategies have been proposed to achieve a smooth surface but a high-crystallinity perovskite film, including component engineering, solvent engineering, interface modification, and optimized preparation process.[18,20–34]

Nevertheless, challenges remain to achieve high-performance PVSCs. On one hand, a large number of defects are inevitably formed at grain boundaries, resulting in serious nonradiative charge recombination and a short carrier life.[35–39] As a result, tremendous efforts have been focused on amending the defect states *via* a variety of strategies, *e.g.*, passivation of surfaces and interfacial defects and passivation of grain boundaries.[17,40–47]

[a] *State Key Laboratory of Silicon Materials, MOE Key Laboratory of Macromolecular Synthesis and Functionalization, Department of Polymer Science and Engineering, Zhejiang University, Hangzhou 310027, P. R. China. E-mail: zjuzlj@zju.edu.cn, hzchen@zju.edu.cn*

[b] *Zhejiang University-Hangzhou Global Scientific and Technological Innovation Center, Hangzhou 310014, P. R. China*

† Electronic supplementary information (ESI) available. See DOI: https://doi.org/10.1039/d2qm01376b

On the other hand, the grain boundary naturally forms a physical gap for smooth charge transport between grains. This is detrimental to charge collection and causes a low fill factor (FF) and poor PCE, but has been less studied.

The most direct way to alleviate the poor grain boundary-induced charge transport issue is *via* enlarging the grain size, and ideally, the grain size should be large enough to connect the anode and cathode within one single grain.[17,48,49] Therefore, a large grain size comparable or larger than the scale of film thickness is required, and the optimal thickness of the perovskite should be limited by the grain size. However, the critical balance between the high crystallinity and surface smoothness determines the grain size around 500–1000 nm.[50] This might be the reason underpinning the limit of perovskite thickness of 500–1000 nm for the optimal devices. However, PVSCs with both high performance and a thick perovskite layer (or good thickness tolerance) are essential for industrial manufacturing with up-scaled fabrication processing, *e.g.*, doctor blade, slot-die, *etc.*, which inevitably cause fluctuation in perovskite thickness.[51] To resolve this issue, it is necessary to dwell on the inter-grain charge transport in multi-crystalline perovskite films and increase their carrier transit lengths.[26,36,37,52–56] However, few efforts have focused on this, due to the lack of fundamentals on the inter-grain charge transport and the shortage of appropriate strategies to bridge the charge transport.[42]

In this work, different from common logic of grain boundary passivation to suppress the charge recombination in perovskite films, we focus on remedying the inter-grain charge transport *via* organic semiconductors to enable thickness-insensitive PVSCs for practical application. We have proposed the concept of a "flat band" quantum well structure (FBQW), that is, the highest occupied molecular orbital (HOMO) and the lowest unoccupied molecular orbital (LUMO) of organic semiconductors are in line with the valence band (VB) and the conductivity band (CB) of the perovskite, respectively, to enable efficient inter-grain charge transport. Non-fullerene acceptors (NFAs) with different energy levels, *i.e.*, HFO-PCIC, HF-PCIC, and OF-PCIC (Fig. 1a), have been blended into perovskite films, and these NFAs are expected to be compelled to the grain boundary during the crystallization of perovskite films.[57] We find that the NFAs have an obvious influence on the series resistance (R_s) of solar cells, and the HFO-PCIC achieves the lowest R_s and the best PCE of over 21%. Moreover, PVSCs with a FBQW structure show very good thickness tolerance, and the efficiency is maintained at 20.7% with the thickness exceeding 1500 nm, which represents the best result among thick PVSCs. Our work proposes the concept of a

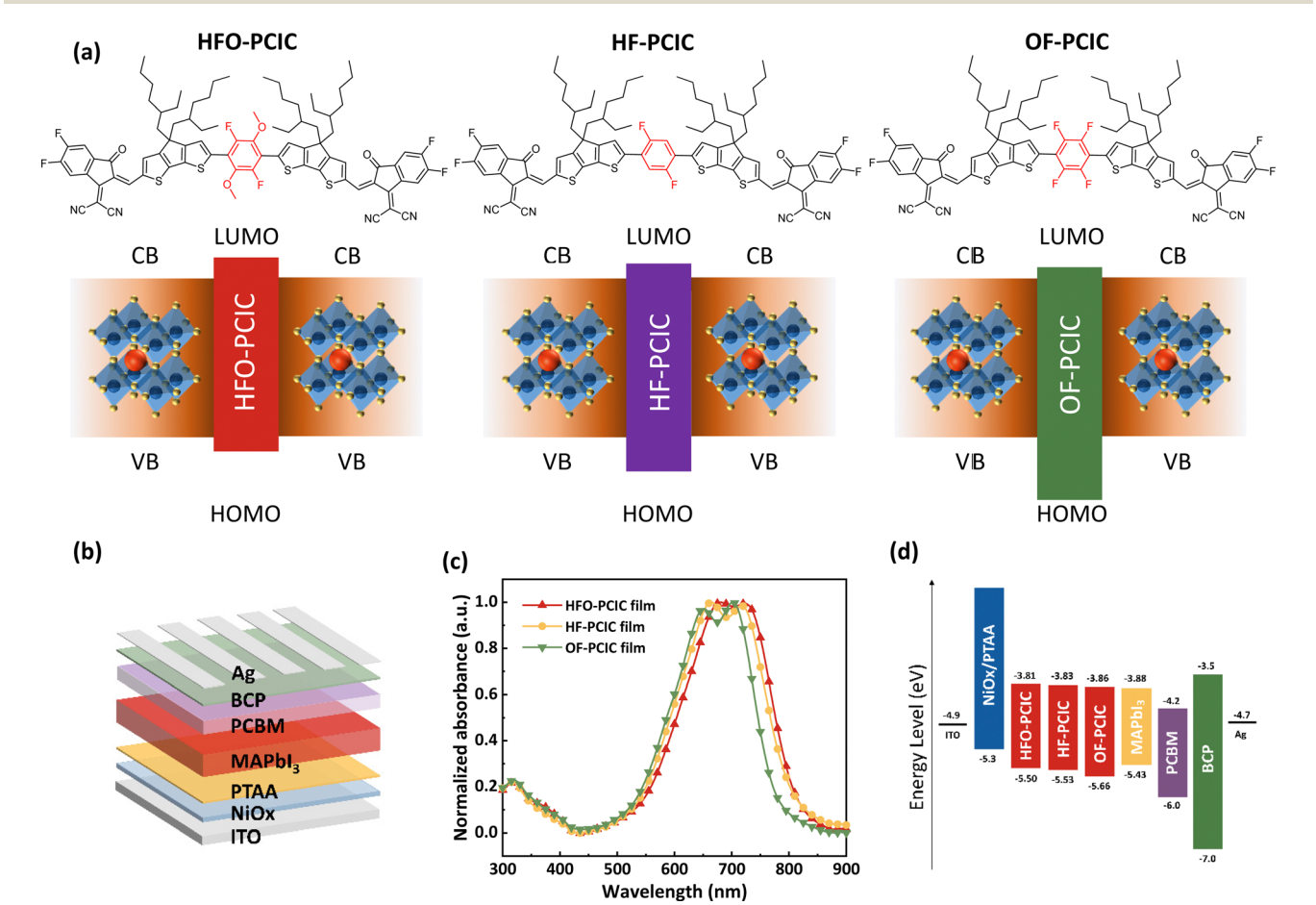

Fig. 1 (a) Chemical structures of HFO-PCIC, HF-PCIC, and OF-PCIC. (b) The schematic device structure of a typical $MAPbI_3$ PVSC device. (c) UV-vis absorption spectra of HFO-PCIC, HF-PCIC, and OF-PCIC thin films. (d) The energy level alignment of each layer.

FBQW structure for boosting the inter-grain charge transport and paves the way for the preparation of thickness-insensitive PVSCs for future commercialization.

Results and discussion

Materials selection

To study the effect of organic semiconductors on device performance, the inverted device structure: glass/indium tin oxide (ITO)/nickel oxide (NiO_x)/poly[bis(4-phenyl)(2,4,6-trimethylphenyl)amine] (PTAA)/$MAPbI_3$/[6,6]-phenyl-C_{61}-butyric acid methyl ester ($PC_{61}BM$)/bathocuproine (BCP)/Ag, was adopted, as shown in Fig. 1b. Considering that the energy level alignment between two semiconductors is the key for charge transfer or charge transport, we focus on exploring the effect of energetic structure across the grain boundary of perovskite film on the device performance. To exclude other effects on the device performance of PVSCs, *e.g.*, morphology, chemical interactions between perovskite and different functional groups,[29] *etc.*, these molecules should have similar chemical structures but different energy levels, which can be tuned *via* delicate modification on the side chains or side groups. As a result, we have carefully selected the home-made NFAs, *i.e.*, HFO-PCIC, HF-PCIC and OF-PCIC from a large pool of organic semiconductors.[57] As shown in Fig. 1c, the absorbing edges of HFO-PCIC, HF-PCIC, and OF-PCIC are 815 nm, 810 nm, and 780 nm, respectively, which are similar enough to exclude the effect of band gap (E_g, 1.69 eV, 1.70 eV, and 1.80 eV) on the optoelectronic properties. It should be noted that the band gap of these organic semiconductors is quite similar to that of the $MAPbI_3$ perovskite film. With the different side groups, these molecules show different HOMO and LUMO levels, as shown in Fig. 1d. Notably, the HFO-PCIC shows the HOMO at −3.81 eV, and the LUMO at −5.50 eV and these values are quite close to the VB and CB of $MAPbI_3$, respectively.[57,58] The HF-PCIC shows overall down-shifted HOMO and LUMO to −3.83 and −5.53 eV, respectively, due to the removal of the electron donating group. The OF-PCIC shows even down-shifted HOMO and LUMO to −3.86 eV and −5.66 eV, respectively. The energy offsets between the LUMO of these NFAs and CB of $MAPbI_3$ perovskite ($\Delta E_{\text{LUMO-CB}}$) are quite small, *i.e.*, 0.07, 0.05 and 0.02 eV for HFO-PCIC, HF-PCIC and OF-PCIC, respectively. While the energy offsets between the NFA HOMO and VB of perovskite ($\Delta E_{\text{HOMO-VB}}$) are large, *i.e.*, 0.07, 0.10, and 0.23 eV for HFO-PCIC, HF-PCIC and OF-PCIC, respectively. It is obvious that these molecules can form different energetic structures with the perovskite at the grain boundary, *i.e.*, the type I quantum well structure with different energy barriers.

Device performance

Therefore, these molecules provide a straightforward comparison to test the effect of the energetic barrier of the grain boundary on the device performance of PVSCs. Fig. 2a shows the current–voltage (*J*–*V*) of PVSC without or with different NFAs, and the detailed device parameters are summarized in Table 1. The PVSCs without any NFAs (or the control device) reach the best PCE of 20.67% (average PCE: 20.10%), with open circuit voltage (V_{OC}) of 1.08 eV, short circuit current density (J_{SC}) of 22.86 mA cm^{-2} and fill factor (FF) of 81.55%. With the HFO-PCIC blended into the perovskite film, which shows both small $\Delta E_{\text{HOMO-VB}}$ and $\Delta E_{\text{LUMO-CB}}$, the device exhibits the best device performance of 21.19% (average PCE: 20.44%), with a V_{OC} of 1.08 eV, J_{SC} of 23.29 mA cm^{-2} and FF of 80.88%. With the OF-PCIC blended into the perovskite film, which shows small $\Delta E_{\text{LUMO-CB}}$ but larger $\Delta E_{\text{HOMO-VB}}$, the devices show the best device performance of 20.47% (average PCE: 19.94%), with a V_{OC} of 1.08 eV, J_{SC} of 22.94 mA cm^{-2} and FF of 80.59%. While the device performance of PVSCs with HF-PCIC sits in between that of the OF-PCIC and HFO-PCIC. From the variation trend, it is concluded that the device performance shows an increasing trend with the $\Delta E_{\text{HOMO-VB}}$ decreasing. These results suggest the interfacial energetic structures indeed play a critical role in determining the device performance of PVSCs. Theoretically, the effect of $\Delta E_{\text{HOMO-VB}}$ and $\Delta E_{\text{LUMO-CB}}$ on the device performance of PVSCs should be similar. However, considering the $\Delta E_{\text{LUMO-CB}}$ are quite small in all cases, the variation of device performance is attributed to the $\Delta E_{\text{HOMO-VB}}$. Interestingly, we find the device stability is increased after NFA modification, as shown in Fig. S6 (ESI†).

It should be noted that, with the $\Delta E_{\text{HOMO-VB}}$ increasing from 0.07 to 0.23 eV, J_{SC} shows a decreasing trend. To determine the detailed mechanism underlying the improved charge generation with smaller $\Delta E_{\text{HOMO-VB}}$, the external quantum efficiency (EQE) of the PVSCs with and without NFAs is measured, as shown in Fig. 2b. It is observed that with the $\Delta E_{\text{HOMO-VB}}$ decreasing, the shape of the EQE spectrum shows little change, while the photo-to-electron response increases over the entire range. Besides, we find the UV-visible absorption spectra of the perovskite films without or with different NFAs addition exhibit very small changes, and this excludes the role of absorption on the improved charge generation, as shown in Fig. S1 in the ESI.† Alternatively, these results support the argument that the addition of NFAs majorly increases the charge generation by affecting the carrier dynamic process or the internal quantum efficiency, rather than any optical effect. By integrating the EQE over the AM 1.5G standard spectrum, the J_{SC}s of the control and the PVSCs blended with HFO-PCIC, HF-PCIC, and OF-PCIC are calculated to be 22.18, 22.83, 22.20 and 21.79 mA cm^{-2}, respectively. These results are in accord with the measured J_{SC} under the solar simulator (within 5%), validating the measured device performance as shown in Table 1. It is obvious that lowering the energetic offset at the grain boundary can greatly affect the carrier dynamics of the PVSCs, particularly the charge transport properties.

Charge transport

To further probe the effect of NFA treatment, we carried out steady-state photoluminescence (PL) spectroscopy and time-resolved photoluminescence (TRPL) decay measurements to examine the possible passivation effect. However, as shown in Fig. S5 and Table S4 (ESI†), neither the PL intensity nor the PL life time show any difference with or without the NFA

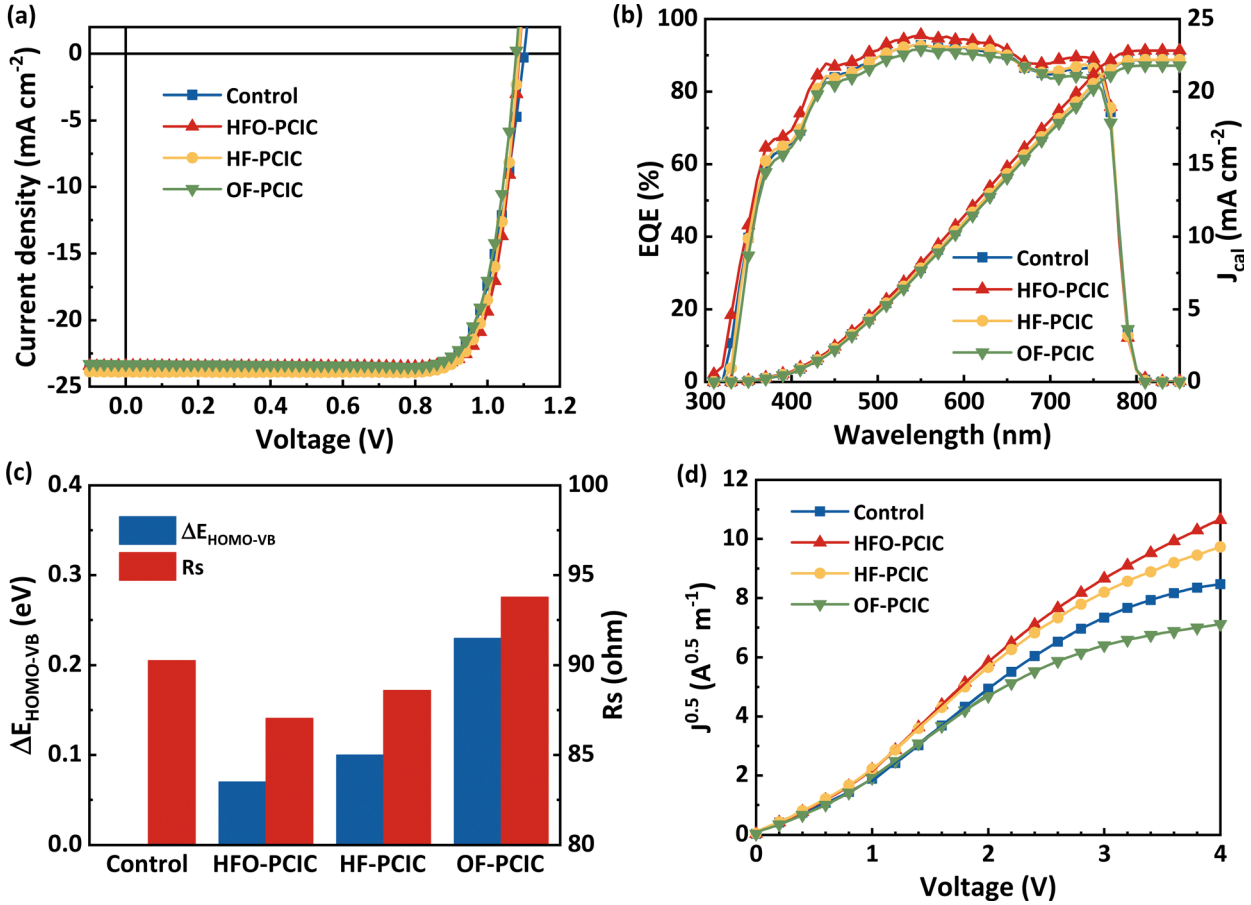

Fig. 2 (a) J–V characteristics of the control and the NFA-mixed PVSCs. (b) EQE spectra and integrated J_{SC} curves of the control and the NFA-mixed PVSCs. (c) The histogram of $\Delta E_{HOMO\text{-}VB}$ and R_s. (d) $J^{0.5}$–V characteristics of hole-only devices, along with linear fits.

modification. These results exclude the possibility of defect passivation as the mechanism for device performance improvement. As a result, we investigated the effect of NFAs on the charge transport of PVSCs. The R_s is the most direct parameter to examine the charge transport properties of the PVSCs. The variation of the R_s with the different NFAs or the $\Delta E_{HOMO\text{-}VB}$ offsets is shown in Fig. 2c. The R_s of the control PVSC device is 90.26 Ω. After blending with the NFAs, the R_s of the PVSCs is 87.02 Ω, 88.55 Ω cm^{-2}, and 93.36 Ω cm^{-2} with the HFO-PCIC, HF-PCIC, and OF-PCIC, respectively (or the increasing $\Delta E_{HOMO\text{-}VB}$ offset: 0.07 eV, 0.10 eV and 0.23 eV, respectively). Therefore, it is concluded that the low $\Delta E_{HOMO\text{-}VB}$ offset will enhance the charge transport.

To further examine the charge transport properties, we can record the carrier mobility of PVSCs *via* space charge limiting current (SCLC) measurement. Considering the charge transport is majorly determined by the $\Delta E_{HOMO\text{-}VB}$ offset, the hole-only device (device structure: ITO/poly(3,4-ethylenedioxythiophene):polystyrene sulfonate (PEDOT:PSS)/$MAPbI_3$/2,2′,7,7′-tetrakis[*N*,*N*-di(4-methoxyphenyl)amino]- 9,9′-spirobi[fluorene] (spiro-OMeTAD)/Ag) is fabricated to measure the hole mobility, and study the effect of different NFAs on the hole mobility. Fig. 2d shows the J–V characteristic curves of the hole-only perovskite device without or with different NFAs. The carrier mobility of the PVSC is calculated by conforming to the formula of

$$J = \frac{\frac{9}{8}\varepsilon\varepsilon_0\mu}{L^3}V^2 \quad (1)$$

where ε (= 32) and ε_0 (= 8.85 × 10^{-12} F m^{-1}) are the relative dielectric constants of $MAPbI_3$ and the vacuum permittivity, respectively. L is the thickness of the perovskite layer on PEDOT:PSS,

Table 1 Photovoltaic performances of PVSCs under AM 1.5 G illumination (100 mW cm^{-2}). The average values were obtained from 30 cells

NFA	$\Delta E_{HOMO\text{-}VB}$ (eV)	V_{OC} (V)	J_{SC} (mA cm^{-2})	FF (%)	R_s (Ω cm^{-2})	PCE (%)	Best PCE (%)	J_{cal} (mA cm^{-2})
Control	0	1.08 ± 0.013	22.86 ± 0.37	81.55 ± 1.52	90.26 ± 5.12	20.10 ± 0.20	20.67	22.18
HFO-PCIC	0.07	1.08 ± 0.005	23.29 ± 0.25	80.88 ± 0.90	87.02 ± 5.46	20.44 ± 0.29	21.19	22.83
HF-PCIC	0.10	1.08 ± 0.013	23.33 ± 0.25	80.18 ± 1.16	88.55 ± 8.79	20.15 ± 0.43	21.09	22.20
OF-PCIC	0.23	1.08 ± 0.005	22.94 ± 0.34	80.59 ± 0.72	93.36 ± 6.76	19.94 ± 0.34	20.47	21.79

Table 2 The hole mobility mobilities of PVSCs

NFA	$\Delta E_{HOMO\text{-}VB}$ (eV)	Hole mobility (10^{-4} cm^2 V^{-1} s^{-1})	R_s (Ω cm^{-2})
None	0	1.88	90.26
HFO-PCIC	0.07	2.68	87.02
HF-PCIC	0.10	2.37	88.55
OF-PCIC	0.23	1.54	93.36

which is around 700 nm, as measured by the profiler. The calculated carrier mobilities are summarized in Table 2. As shown, the hole mobility of the control perovskite device is 1.88 $\times$ 10^{-4} cm^2 V^{-1} s^{-1}. While the hole mobility of the device changed a lot with blending HFO-PCIC, HF-PCIC, and OF-PCIC, which are 2.68 $\times$ 10^{-4} cm^2 V^{-1} s^{-1}, 2.37 $\times$ 10^{-4} cm^2 V^{-1} s^{-1}, and 1.54 $\times$ 10^{-4} cm^2 V^{-1} s^{-1}, respectively. The HFO-PCIC and HF-PCIC, which exhibit small $\Delta E_{HOMO\text{-}VB}$ less than 0.1 eV, can obviously improve the carrier mobility, while the OF-PCIC (higher $\Delta E_{HOMO\text{-}VB}$ $\sim$ 0.23 eV) decreases the carrier mobility, compared to the control device. These results suggest the $\Delta E_{HOMO\text{-}VB}$ offset will greatly affect the hole mobility. In a similar logic, the $\Delta E_{LUMO\text{-}CB}$ offset, which is very small for all the NFAs, is not expected to affect electron mobility, which can be proved with the electron mobility measurement, as shown in Fig. S2 and Table S1 (ESI†). Therefore, we argue that building the FBQW structure can be an important strategy for remedying the inter-grain charge transport in perovskite film for high device performance. Therefore, these results provide a proof of concept that the FBQW structure is useful to enhance the carrier mobility of the PVSCs.

Morphology

Considering that the morphology also affects the charge transport greatly, scanning electron microscopy (SEM) measurements were performed to investigate the morphology of the perovskite film. Fig. 3 shows the surface morphology of the perovskite films without and with different NFAs. All films have large grain sizes, and the surface structure has no significant change. These results exclude the possibility of morphology effect on the carrier mobility variation with different NFA additions.

For a PVSC device, the vertical charge transport plays a dominant role in determining the charge collection, rather than the lateral charge transport. Therefore, we have studied the cross-section morphology of the PVSCs. As shown in Fig. 3, all the perovskite films without or with different NFAs show large grains, which connect the electron transport layer (ETL) and hole transport layer (HTL). This means the inter-grain charge transport will not be a very severe issue for the PVSCs with optimized thickness, which is comparable with the grain size. On the other hand, the inter-grain charge transport might be the reason underlying the thickness limit of the optimal PVSCs.

PVSCs with a thick active layer

It is obvious that the inter-grain will become more and more important for the thicker film, because the number of grain boundaries increases significantly, with the increase of thickness.[59] To amplify the role of NFAs on the device performance of PVSCs and take a further look into the effect of inter-grain energetic structure, it is necessary to create more vertical charge transporting "gaps" or grain boundaries. Therefore, PVSCs with a thick perovskite layer of over 1500 nm thick were fabricated. Fig. 4a shows the *J*–*V* characteristic curves of the PVSCs with a thick active layer (1500 nm), and their device parameters are summarized in Table 3. Fig. 4b shows PCE and R_s distribution statistics of the PVSCs with the perovskite layer over 1500 nm. As shown, after increasing the thickness of the perovskite active layer to 1500 nm, the device performance of the control PVSCs decreases rapidly, with the averaged efficiency dropping from 20.10% (700 nm) to 17.10% (1500 nm) and the best efficiency from 20.67% (700 nm) to 19.60% (1500 nm). For the PVSCs with HFO-PCIC modification, the device performance drop is significantly alleviated with the thickness increasing from 700 nm to 1500 nm. Specifically, with HFO-PCIC incorporation, the averaged efficiency of 1500 nm PVSCs shows an average efficiency of 19.19% and best efficiency of 20.75%, which are comparable to the control device (700 nm), 20.10% and 20.67%, respectively. The variation in device performance is in good agreement with that in R_s, as shown in Fig. 4b. The use of HFO-PCIC decreases the R_s of PVSCs with 1500 nm thickness. Similarly, the addition of OF-IPCIC increases the R_s and harms the device performance, as shown in Table S3 (ESI†). These results confirm the unique advantage of HFO-PCIC or the FBQW structure for improving the charge transport across the grain boundary, which enables good tolerance on the thickness for future commercialization with robust manufacturing.

Horizontal charge transport

Compared to the vertical charge transport, the charge carriers will have to cross a greater grain boundary "gap" when transporting laterally, and this provides a good platform to further test the efficacy of the NFAs or the grain boundary energetic structure on the charge transport properties of the perovskite film.

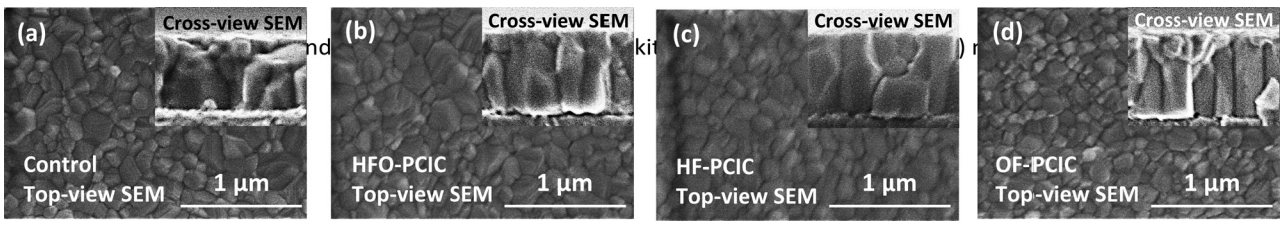

Fig. 3 SEM top-view images and cross-view images of perovskite active layers mixed with (a) none, (b) HFO-PCIC, (c) HF-PCIC, and (d) OF-PCIC.

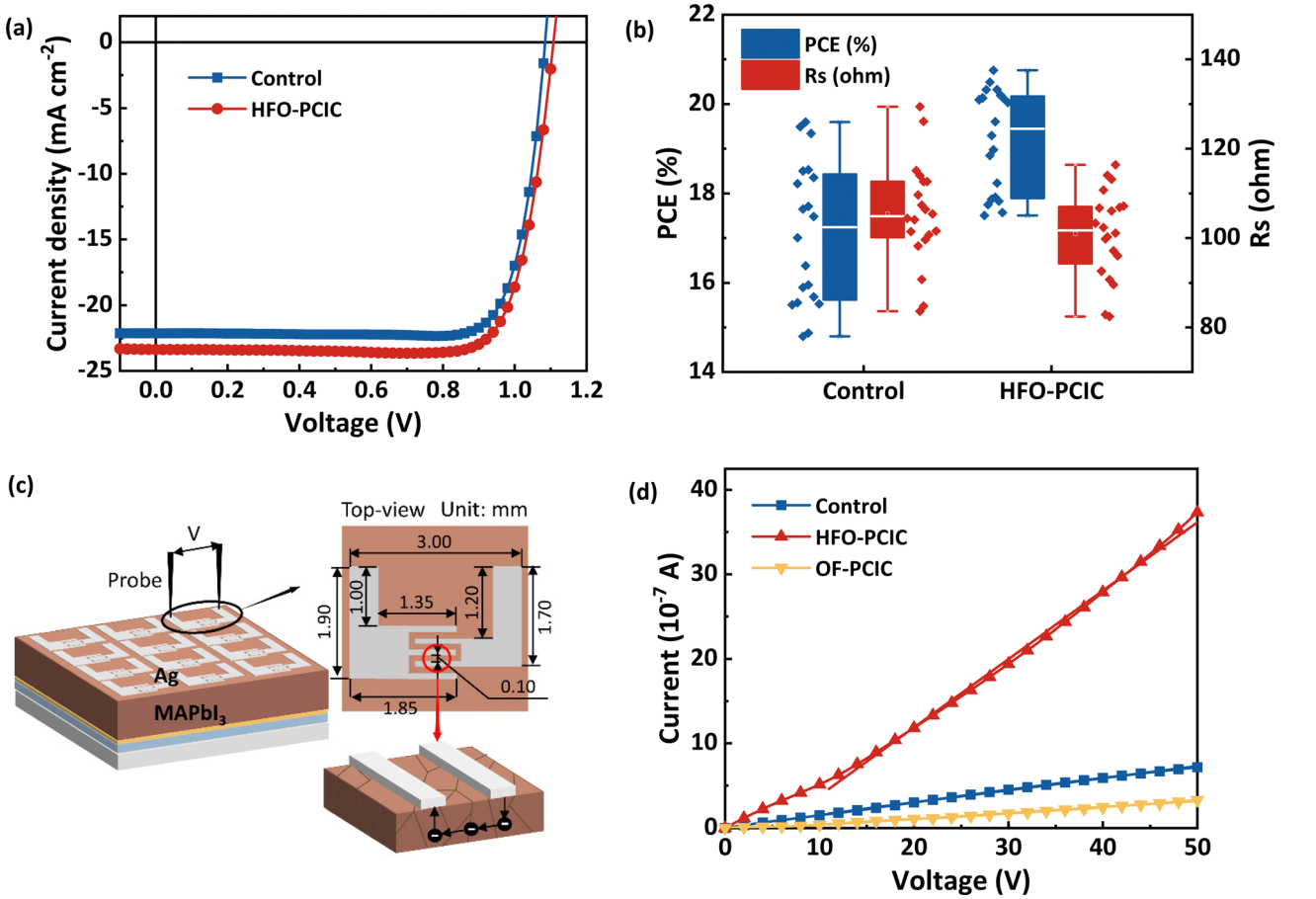

Fig. 4 (a) *J*–*V* characteristics. (b) PCE and R_s distribution statistics of the PVSCs with the perovskite layer over 1500 nm. (c) The diagrammatic sketch of the test process of the horizontal charge transport. (d) *I*–*V* characteristics of the PVSCs in a horizontal transmission test.

Table 3 Photovoltaic performances of PVSCs over 1500 nm under AM 1.5 G illumination (100 mW cm^{-2}). The average values were obtained from 20 cells

NFA	$\Delta E_{HOMO\text{-}VB}$ (eV)	V_{OC} (V)	J_{SC} (mA cm^{-2})	FF (%)	R_s (Ω cm^{-2})	PCE (%)	Horizontal carrier mobility (cm^2 V^{-1} s^{-1})
None	0	1.07	20.09	79.65	105.39	17.10 ± 1.54	0.18
HFO-PCIC	0.07	1.095	22.185	78.99	100.95	19.19 ± 1.12	1.03

Therefore, to further study the effect of inter-grain energetic structure on the charge transport behaviors, we have measured the horizontal charge transport of the perovskite film/device. The schematic diagram of the test method is shown in Fig. 4c, and the device structure involves glass/NiO_x/PTAA/$MAPbI_3$. The resistivity of perovskite film is measured at low bias voltage, where the low injection current will cause a very small disturbance on band structure variation. Therefore, in this region, the carrier mobility can be simply derived from the resistivity of the perovskite, using the following equations:

$$\rho = R\frac{S}{L} = \frac{1}{\sigma} = \frac{1}{en\mu} \quad (2)$$

where ρ is the resistivity, R is the electrical resistance, S is the cross-sectional area of the tested perovskite (= 4.9 × 10^{-10} m^2), L is the length of the charge transport along the tested perovskite (= 0.1 mm), σ is the electrical conductivity, e is the elementary charge (= 1.6 × 10^{-19} C), n is the carrier density (= 10^{15} cm^{-3}),[19] and μ is the carrier mobility. The *I*–*V* characteristic curves of the PVSCs without or with HFO-PCIC and OF-PCIC are shown in Fig. 4d. The $MAPbI_3$ perovskite film without any NFAs exhibits mobility of 0.18 cm^2 V^{-1} s^{-1}. As listed in Table 3, by blending with the HFO-PCIC, which forms a low charge transporting barrier FBQW structure, the carrier mobility increases to 1.03 cm^2 V^{-1} s^{-1}. While with blending OF-PCIC, which forms a high charge transporting barrier, the carrier mobility decreases to 0.09 cm^2 V^{-1} s^{-1}. This result is consistent with the device performance and the SCLC results but is more explicit and amplified. Therefore, this result further confirms that the addition of suitable NFAs to form the FBQW structure could remedy the grain boundaries for smooth charge transport and high device performance with good thickness tolerance.

Discussion

The fundamentals of FBQW are based on the electron tunneling effect. At a spaced interface, the electron can directly hop over the gap when the distance is short. The electron tunneling current between the adjacent perovskite crystal is determined by both the distance and the energy offset, as conforms to the following equation:

$$I \propto A \times e \times V \times \exp\left(-2\frac{\sqrt{2m\Phi}}{\hbar}d\right) \quad (3)$$

where A is a constant, which is relevant to the nature of the materials, surrounding conditions, and the geometry of the quantum well, m is the electron mass, Φ is the barrier height, d is the barrier distance, $\hbar$ is Planck's constant, e is the electron charge, and V is the applied voltage. For the perovskite film, Φ is determined by the energy offset between the perovskite and the matters at the grain boundary, which might be excessive PbI_2, MAI or vacancy before any modification at the grain boundary. Therefore, this Φ is expected to be very large. However, the use of NFAs with energy levels aligning with perovskite crystal will dramatically reduce the Φ, and thus, remedy the charge transport between the grain boundary significantly.

Experimental

Materials

All commercial materials were used as received without further purification. ITO glass (sheet resistance $\leq 10\ \Omega\ cm^2$) and methylammonium iodide (MAI, 99%) were ordered from MaterWin. PbI_2 (99%), $PC_{61}BM$, (99.5%), PTAA (99%) and Spiro-MeOTAD were purchased from Xi'an Polymer Light Technology Corp. Ethylenediamine, ethylene glycol, *N*,*N*-dimethylformamide (DMF, 99%) and BCP (99%) were purchased from TCI. PEDOT:PSS aqueous solution (Al 4083) was purchased from Baytron. 1-Methyl-2-pyrrolidinone (NMP, 99.9%), toluene (99%), nickel nitrate ($Ni(NO_3)_2{\cdot}6H_2O$) and chlorobenzene (99%) were purchased from Aldrich. Ethanol was purchased from Aladdin. Silver (Ag, 99.99%) was purchased from commercial sources.

Device fabrication

ITO glass was washed successively in detergent, deionized water, acetone, isopropanol, and ethanol for 15 minutes, respectively. Then, the substrates were dried in an air oven at a temperature of 100 °C. After ITO glass was treated with ultraviolet ozone for 20 minutes, NiO_x precursor solution ($Ni(NO_3)_2{\cdot}6H_2O$/ethylenediamine = 1/1 M/M) was spin-coated on ITO glass at 4000 rpm for 30 s, calcining at 120 °C and 315 °C for 30 minutes and 60 minutes, respectively. Then all the next steps were carried out in a glove box, where the moisture content was roughly equivalent to 0% (0.5 ppm). A thin layer of PTAA (1 mg mL^{-1} in toluene) was spin-coated onto NiO_x substrate at 6000 rpm for 30 s, then transferred to a hot plate at 100 °C for annealing for 15 minutes. Before spin-coating, the perovskite active layer, the prepared substrate and perovskite precursor solution (1.2 M, MAI/PbI_2 = 1/1 M/M in DMF/NMP = 4/1 v/v) were heated at 70 °C for 20 minutes. To prepare high-quality perovskite film, the substrate was quickly moved to the spin coater, then 60 μL hot precursor solution was dropped onto the substrate. The spin-coating process of perovskite includes two stages. In the first stage, the spinning speed is 1000 rpm, the coating time is 5 s, and the acceleration is 500 rpm s^{-1}. In the second stage, the spinning speed is 6000 rpm, the coating time is 40 s, and the acceleration is 3000 rpm s^{-1}. Importantly, 120 μL of toluene was added to the substrate after 4 s of the second stage of spin coating. Finally, the substrate was moved to a hot plate at 100 °C for annealing for 2 minutes. When the active layer has been prepared, $PC_{61}BM$ (15 mg mL^{-1} in chlorobenzene) and BCP (1 mg mL^{-1} in ethanol) was added to the substrate successively at 3000 rpm for 30 s, respectively. Finally, the finished samples were transferred to the evaporation chamber to deposit 100 nm Ag.

The fabrication process of over 1500 nm devices is consistent with the description above, but the concentration of perovskite precursor solution has changed to 2.0 M. The concentration of NFAs in perovskite precursor solution is the respective saturation concentration in DMF, and the relationship between the additive amount and the PCE is shown in Fig. S4 (ESI†).

For the horizontal charge transport test, the configuration of the PVSCs is glass/NiO_x/PTAA/$MAPbI_3$ and the preparation method of each layer is the same as that mentioned above.

Characterization

The *J*–*V* measurement was performed on the solar simulator (SS-X50, Enlitech) along with AM 1.5G spectra whose intensity was calibrated by the certified standard silicon solar cell (KG2, Enlitech) at 100 mW cm^2. The mismatch value is between 0.997 and 1.003. The area of the device was defined as 0.05979 cm^2 by the certified metal mask. EQE data were measured *via* the solar-cell spectral-response measurement system (QE-R, Enlitech). UV-vis absorption spectra were recorded on a Shimadzu UV-1800 spectrophotometer. SEM images were obtained from a Hitachi S-4800. The *I*–*V* curves in the horizontal charge transport were obtained by the semiconductor parameter analyzer (Keysight B1500A). PL and TRPL spectra were obtained using an FLSP920 spectrofluorometer at an excitation wavelength of 515 nm. The device for the stability test is stored in the N_2 glove box without package.

Conclusions

To sum up, we modified the perovskite inter-grain energetic structure *via* an organic semiconductor and investigated the effects on the charge transport properties of perovskite film and the device performance of perovskite solar cells (PVSCs). In particular, we have proposed that a ''flat band'' quantum well structure (FBQW, where the HOMO and LUMO of the organic semiconductor are aligned with the VB and CB of the perovskite, respectively) can effectively improve the charge transport across grain boundaries, and results in a high device performance of over 21% for $MAPbI_3$ PVSCs. Moreover, this strategy or concept breaks the thickness limit of the optimal device

(similar to the grain boundary and less than 1000 nm) and enables good thickness tolerance. Therefore, with the FBQW energetic structure, the PVSCs with 1500 nm perovskite layer exhibit the best efficiency of 20.75%, which is among the best for thick film PVSCs. The effects of inter-grain energetic structure on the charge transport of perovskite film and the efficacy of the FBQW are further studied and confirmed *via* the space-charge-limited-current measurement, and these effects are amplified with the horizontal charge transport device structure. Therefore, our work proposes a novel concept/strategy of FBQW structure to remedy the inter-grain charge transport and enables good thickness tolerance for future commercialization of PVSCs.

Author contributions

L. Z. conceived the idea and proposed the concept of a FBQW structure. L. Z. and Y. C. designed the experiments. Y. C. completed the device fabrication. Y. C., F. W., C. X. and H. W. contributed to the result analysis. S. L. synthesized the HFO-PCIC, HF-PCIC and OF-PCIC. T. C. performed morphology characterization. X. W., B. P. and H. L. performed the horizontal charge transport measurements. Y. C. and L. Z. prepared the manuscript. L.Z. and H.C. supervised this work. All authors commented on the manuscript.

Conflicts of interest

There are no conflicts to declare.

Acknowledgements

This work was supported by the Fundamental Research Funds for the Central Universities (No. 226-2022-00133 and No. 226-2022-00209), the ''Pioneering'' and ''Leading Goose'' R&D Program of Zhejiang (2022C01104), the research start up fund from Zhejiang University, and the National Natural Science Foundation of China (No. 52127806, 52173185, 21734008, and 61721005).

Notes and references

1 Q. Dong, Y. Fang, Y. Shao, P. Mulligan, J. Qiu, L. Cao and J. Huang, Electron-hole diffusion lengths >175 um in solution-grown $CH_3NH_3PbI_3$ single crystals, *Science*, 2015, **347**, 967–970.

2 D. W. deQuilettes, S. M. Vorpahl, S. D. Stranks, H. Nagaoka, G. E. Eperon, M. E. Ziffer, H. J. Snaith and D. S. Ginger, Impact of microstructure on local carrier lifetime in perovskite solar cells, *Science*, 2015, **348**, 683–686.

3 S. D. Stranks, G. E. Eperon, G. Grancini, C. Menelaou, M. J. P. Alcocer, T. Leijtens, L. M. Herz, A. Petrozza and H. J. Snaith, Electron-Hole Diffusion Lengths Exceeding 1 Micrometer in an Organometal Trihalide Perovskite Absorber, *Science*, 2013, **342**, 341–344.

4 B. Yan, X. Liu, W. Lu, M. Feng, H. Yan, Z. Li, S. Liu, C. Wang, J. Hu and D. Xue, Indoor photovoltaics awaken the world's first solar cells, *Sci. Adv.*, 2022, **8**, eadc9923.

5 Y. Jiang, C. Sun, J. Xu, S. Li, M. Cui, X. Fu, Y. Liu, Y. Liu, H. Wan, K. Wei, T. Zhou, W. Zhang, Y. Yang, J. Yang, C. Qin, S. Gao, J. Pan, Y. Liu, S. Hoogland, E. H. Sargent, J. Chen and M. Yuan, Synthesis-on-substrate of quantum dot solids, *Nature*, 2022, **612**, 679–684.

6 L. Zuo, X. Shi, W. Fu and A. K. Jen, Highly Efficient Semitransparent Solar Cells with Selective Absorption and Tandem Architecture, *Adv. Mater.*, 2019, **31**, 1901683.

7 Z. Li, B. Li, X. Wu, S. A. Sheppard, S. Zhang, D. Gao, N. J. Long and Z. Zhu, Organometallic-functionalized interfaces for highly efficient inverted perovskite solar cells, *Science*, 2022, **376**, 416–420.

8 R. He, S. Ren, C. Chen, Z. Yi, Y. Luo, H. Lai, W. Wang, G. Zeng, X. Hao, Y. Wang, J. Zhang, C. Wang, L. Wu, F. Fu and D. Zhao, Wide-bandgap organic–inorganic hybrid and all-inorganic perovskite solar cells and their application in all-perovskite tandem solar cells, *Energy Environ. Sci.*, 2021, **14**, 5723–5759.

9 C. H. Liao, C. H. Chen, J. Bing, C. Bailey, Y. T. Lin, T. M. Pandit, L. Granados, J. Zheng, S. Tang, B. H. Lin, H. W. Yen, D. R. McCamey, B. J. Kennedy, C. C. Chueh and A. W. Y. Ho-Baillie, Inorganic-Cation Pseudohalide 2D $Cs_2Pb(SCN)_2Br_2$ Perovskite Single Crystal, *Adv. Mater.*, 2022, **34**, 2104782.

10 H. Wang, X. Gong, D. Zhao, Y.-B. Zhao, S. Wang, J. Zhang, L. Kong, B. Wei, R. Quintero-Bermudez, O. Voznyy, Y. Shang, Z. Ning, Y. Yan, E. H. Sargent and X. Yang, A Multi-functional Molecular Modifier Enabling Efficient Large-Area Perovskite Light-Emitting Diodes, *Joule*, 2020, **4**, 1977–1987.

11 A. Kojima, K. Teshima, Y. Shirai and T. Miyasaka, Organometal Halide Perovskites as Visible-Light Sensitizers for Photovoltaic Cells, *J. Am. Chem. Soc.*, 2009, **131**, 6050–6051.

12 X. Wu, B. Li, Z. Zhu, C. C. Chueh and A. K.-Y. Jen, Designs from single junctions, heterojunctions to multijunctions for high-performance perovskite solar cells, *Chem. Soc. Rev.*, 2021, **50**, 13090–13128.

13 X. Wu, Y. Liu, F. Qi, F. Lin, H. Fu, K. Jiang, S. Wu, L. Bi, D. Wang, F. Xu, A. K.-Y. Jen and Z. Zhu, Improved stability and efficiency of perovskite/organic tandem solar cells with an all-inorganic perovskite layer, *J. Mater. Chem. A*, 2021, **9**, 19778–19787.

14 M. G. Mohamed, C.-C. Lee, A. F. M. EL-Mahdy, J. Lüder, M.-H. Yu, Z. Li, Z. Zhu, C.-C. Chueh and S.-W. Kuo, Exploitation of two-dimensional conjugated covalent organic frameworks based on tetraphenylethylene with bicarbazole and pyrene units and applications in perovskite solar cells, *J. Mater. Chem. A*, 2020, **8**, 11448–11459.

15 X. Li, X. Wu, B. Li, Z. Cen, Y. Shang, W. Lian, R. Cao, L. Jia, Z. Li, D. Gao, X. Jiang, T. Chen, Y. Lu, Z. Zhu and S. Yang, Modulating the deep-level defects and charge extraction for efficient perovskite solar cells with high fill factor over 86%, *Energy Environ. Sci.*, 2022, **15**, 4813–4822.

16 M.-H. Yu, P.-C. Han, C.-C. Lee, I.-C. Ni, Z. Zhu, E. Z. Kurmaev, S. Furukawa, K. C.-W. Wu and C.-C. Chueh, A self-arranged metal–organic polyhedron/fullerene asymmetric structure improves the performance of inverted perovskite solar cells, *J. Mater. Chem. C*, 2022, **10**, 14542–14548.

17 S. Shan, C. Xu, H. Wu, B. Niu, W. Fu, L. Zuo and H. Chen, Manipulating the Crystallization and Phase Transition for High-Performance $CsPbI_2Br$ Solar Cells, *Adv. Energy Mater.*, 2023, **13**, 2203682.

18 S. Shan, Y. Li, H. Wu, T. Chen, B. Niu, Y. Zhang, D. Wang, C. Kan, X. Yu, L. Zuo and H. Chen, Manipulating the film morphology evolution toward green solvent-processed perovskite solar cells, *SusMat*, 2021, **1**, 537–544.

19 Z. Ni, C. Bao, Y. Liu, Q. Jiang, W. Wu, S. Chen, X. Dai, B. Chen, B. Hartweg, Z. Yu, Z. Holman and J. Huang, Resolving spatial and energetic distributions of trap states in metal halide perovskite solar cells, *Science*, 2020, **367**, 1352–1358.

20 N. J. Jeon, J. H. Noh, W. S. Yang, Y. C. Kim, S. Ryu, J. Seo and S. I. Seok, Compositional engineering of perovskite materials for high-performance solar cells, *Nature*, 2015, **517**, 476–480.

21 N. J. Jeon, J. H. Noh, Y. C. Kim, W. S. Yang, S. Ryu and S. I. Seok, Solvent engineering for high-performance inorganic-organic hybrid perovskite solar cells, *Nat. Mater.*, 2014, **13**, 897–903.

22 N. G. Park, Methodologies for high efficiency perovskite solar cells, *Nano Convergence*, 2016, **3**, 15.

23 H. Zhou, Q. Chen, G. Li, S. Luo, T. Song, H. Duan, Z. Hong, J. You, Y. Liu and Y. Yang, Interface engineering of highly efficient perovskite solar cells, *Science*, 2014, **345**, 542–546.

24 M. Liu, M. B. Johnston and H. J. Snaith, Efficient planar heterojunction perovskite solar cells by vapour deposition, *Nature*, 2013, **501**, 395–398.

25 F. Wu, K. Yan, H. Wu, B. Niu, Z. Liu, Y. Li, L. Zuo and H. Chen, Tuning interfacial chemical interaction for high-performance perovskite solar cell with PEDOT:PSS as hole transporting layer, *J. Mater. Chem. A*, 2021, **9**, 14920–14927.

26 C. Xu, L. Zuo, P. Hang, X. Guo, Y. Pan, G. Zhou, T. Chen, B. Niu, X. Xu, Z. Hong, D. Wang, H. Zhu, X. Yu, D. Yang and H. Chen, Synergistic effects of bithiophene ammonium salt for high-performance perovskite solar cells, *J. Mater. Chem. A*, 2022, **10**, 9971–9980.

27 B. Niu, H. Wu, J. Yin, B. Wang, G. Wu, X. Kong, B. Yan, J. Yao, C.-Z. Li and H. Chen, Mitigating the Lead Leakage of High-Performance Perovskite Solar Cells via In Situ Polymerized Networks, *ACS Energy Lett.*, 2021, **6**, 3443–3449.

28 L. Zuo, Z. Gu, T. Ye, W. Fu, G. Wu, H. Li and H. Chen, Enhanced photovoltaic performance of $CH_3NH_3PbI_3$ perovskite solar cells through interfacial engineering using self-assembling monolayer, *J. Am. Chem. Soc.*, 2015, **137**, 2674–2679.

29 L. Zuo, Q. Chen, N. De Marco, Y. T. Hsieh, H. Chen, P. Sun, S. Y. Chang, H. Zhao, S. Dong and Y. Yang, Tailoring the Interfacial Chemical Interaction for High-Efficiency Perovskite Solar Cells, *Nano Lett.*, 2017, **17**, 269–275.

30 F. Wu, K. Yan, H. Wu, Y. Guo, S. Shan, T. Chen, W. Fu, L. Zuo and H. Chen, Polypropylene Glycol-Modified Anode Interface for High-Performance Perovskite Solar Cells, *Chin. J. Chem.*, 2022, **40**, 2694–2700.

31 L. He, H. Wu, X. Lian, L. Zuo, G. Wu and H. Chen, Efficient and stable inverted perovskite solar cells incorporating 4-Fluorobenzylammonium iodide, *Org. Electron.*, 2021, **92**, 106124.

32 F. U. Kosasih, E. Erdenebileg, N. Mathews, S. G. Mhaisalkar and A. Bruno, Thermal evaporation and hybrid deposition of perovskite solar cells and mini-modules, *Joule*, 2022, **6**, 2692–2734.

33 Q. Jiang, J. Tong, R. A. Scheidt, X. Wang, A. E. Louks, Y. Xian, R. Tirawat, A. F. Palmstrom, M. P. Hautzinger, S. P. Harvey, S. Johnston, L. T. Schelhas, B. W. Larson, E. L. Warren, M. C. Beard, J. J. Berry, Y. Yan and K. Zhu, Compositional texture engineering for highly stable wide-bandgap perovskite solar cells, *Science*, 2022, **378**, 1295–1300.

34 Q. Cheng, H. Chen, F. Yang, Z. Chen, W. Chen, H. Yang, Y. Shen, X. M. Ou, Y. Wu, Y. Li and Y. Li, Molecular Self-Assembly Regulated Dopant-Free Hole Transport Materials for Efficient and Stable n-i-p Perovskite Solar Cells and Scalable Modules, *Angew. Chem., Int. Ed.*, 2022, **61**, 202210613.

35 F. Huang, Y. Dkhissi, W. Huang, M. Xiao, I. Benesperi, S. Rubanov, Y. Zhu, X. Lin, L. Jiang, Y. Zhou, A. Gray-Weale, J. Etheridge, C. R. McNeill, R. A. Caruso, U. Bach, L. Spiccia and Y.-B. Cheng, Gas-assisted preparation of lead iodide perovskite films consisting of a monolayer of single crystalline grains for high efficiency planar solar cells, *Nano Energy*, 2014, **10**, 10–18.

36 H. S. Kim and N. G. Park, Parameters Affecting I-V Hysteresis of $CH_3NH_3PbI_3$ Perovskite Solar Cells: Effects of Perovskite Crystal Size and Mesoporous TiO_2 Layer, *J. Phys. Chem. Lett.*, 2014, **5**, 2927–2934.

37 J. Jeong, M. Kim, J. Seo, H. Lu, P. Ahlawat, A. Mishra, Y. Yang, M. A. Hope, F. T. Eickemeyer, M. Kim, Y. J. Yoon, I. W. Choi, B. P. Darwich, S. J. Choi, Y. Jo, J. H. Lee, B. Walker, S. M. Zakeeruddin, L. Emsley, U. Rothlisberger, A. Hagfeldt, D. S. Kim, M. Gratzel and J. Y. Kim, Pseudo-halide anion engineering for alpha-$FAPbI_3$ perovskite solar cells, *Nature*, 2021, **592**, 381–385.

38 J. Li, L. Zuo, H. Wu, B. Niu, S. Shan, G. Wu and H. Chen, Universal Bottom Contact Modification with Diverse 2D Spacers for High-Performance Inverted Perovskite Solar Cells, *Adv. Funct. Mater.*, 2021, **31**, 2104036.

39 L. Duan and A. Uddin, Defects and stability of perovskite solar cells: a critical analysis, *Mater. Chem. Front.*, 2022, **6**, 400–417.

40 A. R. b Mohd Yusoff, M. Vasilopoulou, D. G. Georgiadou, L. C. Palilis, A. Abate and M. K. Nazeeruddin, Passivation and process engineering approaches of halide perovskite films for high efficiency and stability perovskite solar cells, *Energy Environ. Sci.*, 2021, **14**, 2906–2953.

41 T. Wu, Y. Wang, X. Li, Y. Wu, X. Meng, D. Cui, X. Yang and L. Han, Efficient Defect Passivation for Perovskite Solar

Cells by Controlling the Electron Density Distribution of Donor-π-Acceptor Molecules, *Adv. Energy Mater.*, 2019, **9**, 1803766.

42 T. H. Han, J. W. Lee, C. Choi, S. Tan, C. Lee, Y. Zhao, Z. Dai, N. De Marco, S. J. Lee, S. H. Bae, Y. Yuan, H. M. Lee, Y. Huang and Y. Yang, Perovskite-polymer composite cross-linker approach for highly-stable and efficient perovskite solar cells, *Nat. Commun.*, 2019, **10**, 520.

43 X. Lian, H. Wu, L. Zuo, G. Zhou, X. Wen, Y. Zhang, G. Wu, Z. Xie, H. Zhu and H. Chen, Stable Quasi-2D Perovskite Solar Cells with Efficiency over 18% Enabled by Heat–Light Co-Treatment, *Adv. Funct. Mater.*, 2020, **30**, 2004188.

44 H. Wu, X. Lian, S. Tian, Y. Zhang, M. Qin, Y. Zhang, F. Wang, X. Lu, G. Wu and H. Chen, Additive-Assisted Hot-Casting Free Fabrication of Dion–Jacobson 2D Perovskite Solar Cell with Efficiency Beyond 16%, *Sol. RRL*, 2020, **4**, 2000087.

45 L. Zuo, H. Guo, D. W. deQuilettes, S. Jariwala, N. De Marco, S. Dong, R. DeBlock, D. S. Ginger, B. Dunn, M. Wang and Y. Yang, Polymer-modified halide perovskite films for efficient and stable planar heterojunction solar cells, *Sci. Adv.*, 2017, **3**, 1700106.

46 Y. Huang, K. Yan, B. Niu, Z. Chen, E. Gu, H. Liu, B. Yan, J. Yao, H. Zhu, H. Chen and C.-Z. Li, Finite perovskite hierarchical structures via ligand confinement leading to efficient inverted perovskite solar cells, *Energy Environ. Sci.*, 2023, **16**, 557–564.

47 R. Qiao and L. Zuo, Self-assembly monolayers boosting organic–inorganic halide perovskite solar cell performance, *J. Mater. Res.*, 2018, **33**, 387–400.

48 Y. Guo, H. Wu, Z. Liu, S. Shan, B. Niu, X. Lian, L. Zuo and H. Chen, Manipulating Perovskite Precursor Solidification toward 21% Pristine $MAPbI_3$ Solar Cells, *Sol. RRL*, 2021, **5**, 2100114.

49 L. Zuo, S. Dong, N. De Marco, Y. T. Hsieh, S. H. Bae, P. Sun and Y. Yang, Morphology Evolution of High Efficiency Perovskite Solar Cells via Vapor Induced Intermediate Phases, *J. Am. Chem. Soc.*, 2016, **138**, 15710–15716.

50 M. C. López-González, G. del Pozo, D. Martín-Martín, L. Muñoz-Díaz, J. C. Pérez-Martínez, E. Hernández-Balaguera, B. Arredondo, Y. Galagan, M. Najafi and B. Romero, Evaluation of Active Layer Thickness Influence in Long-Term Stability and Degradation Mechanisms in CsFAPbIBr Perovskite Solar Cells, *Appl. Sci.*, 2021, **11**, 11668.

51 J. Yang, E. L. Lim, L. Tan and Z. Wei, Ink Engineering in Blade-Coating Large-Area Perovskite Solar Cells, *Adv. Energy Mater.*, 2022, **12**, 2200975.

52 Y. Yu, J. Li, D. Geng, J. Wang, L. Zhang, T. L. Andrew, M. S. Arnold and X. Wang, Development of Lead Iodide Perovskite Solar Cells Using Three-Dimensional Titanium Dioxide Nanowire Architectures, *ACS Nano*, 2015, **9**, 564–572.

53 W. Fu, T. Zhao, H. Liu, F. Lin, L. Zuo, X. Li and A. K. Y. Jen, High-Efficiency Quasi-2D Perovskite Solar Cells Incorporating 2,2′-Biimidazolium Cation, *Sol. RRL*, 2021, **5**, 2000700.

54 Z. Zhang, M. Sheri, Z. A. Page, T. Emrick, A. Saeki, Y. Liu and T. P. Russell, Understanding Hole Extraction of Inverted Perovskite Solar Cells, *ACS Appl. Mater. Interfaces*, 2020, **12**, 56068–56075.

55 L. Zuo, Z. Li and H. Chen, Ion migration and accumulation in halide perovskite solar cells, *Chin. J. Chem.*, 2022, **41**, 861–876.

56 W. Cha, W.-Y. Cha, I. Noh, S. Seki, H. Ohkita and D. Kim, Controlling the charge carrier dynamics by modulating the orientation diversity of perovskites, *Mater. Chem. Front.*, 2022, **6**, 1026–1032.

57 S. Li, L. Zhan, W. Zhao, S. Zhang, B. Ali, Z. Fu, T.-K. Lau, X. Lu, M. Shi, C.-Z. Li, J. Hou and H. Chen, Revealing the effects of molecular packing on the performances of polymer solar cells based on A–D–C–D–A type non-fullerene acceptors, *J. Mater. Chem. A*, 2018, **6**, 12132–12141.

58 S. S. Shin, S. J. Lee and S. I. Seok, Exploring wide bandgap metal oxides for perovskite solar cells, *APL Mater.*, 2019, **7**, 022401.

59 J. Chen, L. Zuo, Y. Zhang, X. Lian, W. Fu, J. Yan, J. Li, G. Wu, C.-Z. Li and H. Chen, High-Performance Thickness Insensitive Perovskite Solar Cells with Enhanced Moisture Stability, *Adv. Energy Mater.*, 2018, **8**, 1800438.

